



# Electron-donor/-acceptor ratio-guided molecular engineering for buried interface optimization in n-i-p perovskite solar cells

Hui Duan<sup>1,2</sup>, Jiahui Jin<sup>2</sup>, Xiaoye Liu<sup>2</sup>, Xinxuan Yang<sup>3</sup>, Hongbo Liu<sup>4</sup>, Lin Fan<sup>1,2,5</sup>, Fengyou Wang<sup>1,2,5,\*</sup>, Jinghai Yang<sup>2,5</sup>, Lili Yang<sup>2,5,\*</sup>

## Keywords:

Perovskite solar cells, dipolar molecules, the buried interface, defect passivation, asymmetric molecular engineering

## Citation:

Duan, H.; Jin, J.; Liu, X.; Yang, X.; Liu, H.; Fan, L.; Wang, F.; Yang, J.; Yang, L.

Electron-donor/-acceptor ratio-guided molecular engineering for buried interface optimization in n-i-p perovskite solar cells. *Energy Mater.* 2026, 6, 600031.

<https://dx.doi.org/10.20517/energymater.2025.183>

Received: 30 Oct 2025

First Decision: 16 Dec 2025

Revised: 10 Mar 2026

Accepted: 13 Mar 2026

Published: 7 Apr 2026

## Academic Editor:

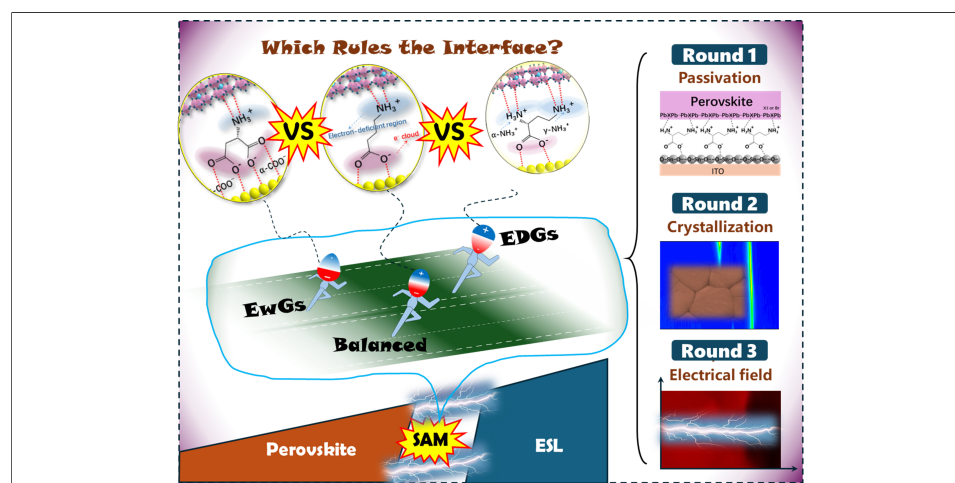
Soo Young Kim

## Copy Editor:

Xing-Yue Zhang

## Production Editor:

Xing-Yue Zhang



## Abstract

The buried interface between the electron transport layer (ETL) and perovskite is critical for the performance of perovskite solar cells (PSCs). Modifying the microstructure of this buried interface using dipolar molecules is among the most effective strategies to enhance device performance. However, the influence of the electron-donating/electron-withdrawing group ratio (EDG/EWG ratio) of dipolar molecules on buried interface engineering has not been systematically investigated. In this work, dipolar molecules are classified into EWG-rich, balanced, and EDG-rich configurations according to their EDG/EWG ratio, using L-aspartic acid, 4-aminobutyric acid, and L-2,4-diaminobutyric acid (DBA) as model systems. We confirm that the primary factor limiting device performance is located on the perovskite side rather than the ETL side. Both experimental and theoretical results reveal that the EDG-rich dipolar configuration provides the most efficient defect passivation for perovskite, promotes the growth of high-quality perovskite films, strengthens the interfacial electric field, and accelerates interfacial electron

<sup>1</sup>Key Laboratory of Preparation and Application of Environmental Friendly Materials, Ministry of Education, Jilin Normal University, Changchun 130103, Jilin, China.

<sup>2</sup>Key Laboratory of Functional Materials Physics and Chemistry of the Ministry of Education, Jilin Normal University, Changchun 130103, Jilin, China.

<sup>3</sup>Changchun Institute of Optics, Fine Mechanics and Physics, Chinese Academy of Sciences, Changchun 130033, Jilin, China.

<sup>4</sup>College of Information Technology, Jilin Normal University, Siping 136000, Jilin, China.

<sup>5</sup>National Demonstration Center for Experimental Physics Education, Jilin Normal University, Siping 136000, Jilin, China.

\*Correspondence to: Prof. Fengyou Wang, Prof. Lili Yang, Key Laboratory of Functional Materials Physics and Chemistry of the Ministry of Education, Jilin Normal University, Changchun 130103, Jilin, China. E-mail: wfy@jlnu.edu.cn; llyang1980@126.com

extraction and transport. As a result, the DBA-modified device achieves a champion PCE of 24.18% and maintains 85% of its initial efficiency after 30 days of ambient storage (20–25 °C, 25%–30% relative humidity) without encapsulation, showing excellent long-term stability. This work establishes asymmetric molecular engineering as a key design principle for optimizing the buried interface in high-performance PSCs.

## INTRODUCTION

Recently, perovskite solar cells (PSCs) have achieved certified power conversion efficiencies (PCEs) exceeding 27% through advances in electron transport layer (ETL) and interfacial engineering<sup>[1–4]</sup>. Tin dioxide (SnO<sub>2</sub>), a prominent inorganic ETL candidate, offers advantages including facile synthesis, suitable work function, and high optical transmittance<sup>[5]</sup>.

However, interfacial issues between SnO<sub>2</sub> and perovskite layers remain critical bottlenecks that limit both efficiency and stability. Three key problems persist at the buried interface: (1) Impurities and lattice vacancies on the SnO<sub>2</sub> surface, together with ionic defects on the perovskite surface, lead to a high defect density at the buried interface - approximately 100 times higher than that within the bulk perovskite layer<sup>[6]</sup>; (2) These defects reduce the built-in electric field, impeding the separation and transport of photogenerated carriers and degrading device performance; (3) The conduction band (CB) offset between SnO<sub>2</sub> and perovskite contributes to hysteresis and limits PCE<sup>[7]</sup>. To address these limitations, three main strategies have been developed: (i) surface functionalization using dipolar molecules (e.g., P-biguanylbenzoic acid HCl<sup>[8]</sup>, 4,4'-diaminodiphenyl sulfone HI<sup>[9]</sup>); (ii) lattice engineering via metal doping (Nb<sup>5+</sup><sup>[10]</sup>, Nd<sup>3+</sup><sup>[11]</sup>, K<sup>+</sup><sup>[12]</sup>); (iii) thermodynamic control through additive engineering (NH<sub>4</sub>F<sup>[13]</sup>).

Zwitterionic dipolar molecules are particularly attractive because their functional groups can passivate buried interfacial defects and introduce an interfacial dipole field, making them highly effective modifiers<sup>[14–17]</sup>. The molecular configurations of these dipolar systems can be classified into three types based on the electron-donating group (EDG)/electron-withdrawing group (EWG) ratio (the EDG/EWG ratio): EWG-rich, balanced, and EDG-rich. These configurations form self-assembled monolayers (SAMs) with different interfacial charge states (negative, neutral, positive), enabling layer-selective passivation at the SnO<sub>2</sub>/perovskite interface. Crucially, the EDG/EWG ratio determines the magnitude of the SAM-induced interfacial dipole field, which fundamentally modulates charge transport dynamics<sup>[18–30]</sup>. Nevertheless, systematic studies on how EDG/EWG asymmetry governs interfacial properties are still lacking. Such investigations are essential for establishing rational design rules for high-performance perovskite solar cells.

Herein, we systematically compare three molecular architectures (EWG-rich, balanced, and EDG-rich) to establish structure-performance relationships, using L-aspartic acid (AA), 4-aminobutyric acid (ABA), and L-2,4-diaminobutyric acid (DBA) as representative models. Experimental and computational analyses show that all three modifiers contribute to interfacial defect passivation, strain relaxation, charge transport, and enhanced device performance. Defect passivation, strain relaxation, interfacial charge transport, and device performance all improve with increasing EDG/EWG ratio. This work systematically establishes structure-performance relationships between the EDG/EWG ratio of dipolar molecules, buried interface engineering, and device photovoltaic performance. We reveal that the perovskite side - rather than the ETL side - acts as the primary factor limiting buried interface performance.

## EXPERIMENTAL

### Fabrication of ETL (SnO<sub>2</sub>, SnO<sub>2</sub>/AA, SnO<sub>2</sub>/ABA, and SnO<sub>2</sub>/DBA) electrodes

The SnO<sub>2</sub> solution was spin-coated onto an ITO substrate at 3,000 rpm for 30 s, then annealed at 150 °C for 30 min and cooled to room temperature. Interfacial modification materials (AA, ABA, DBA) were dissolved in deionized water at an optimal concentration of 0.5 mg·mL<sup>-1</sup>. Then, 100 µL of AA, ABA, or DBA aqueous solution was spin-coated onto the SnO<sub>2</sub> film at 3,000 rpm for 30 s and annealed at 100 °C for 5 min. Detailed materials, device fabrication, and characterization procedures are provided in the [Supplementary Materials](#).

### Characterization methods

Density Functional Theory (DFT) calculations were performed using the Projector-Augmented Wave method through the Vienna ab initio Simulation Package (VASP). X-ray photoelectron spectroscopy (XPS) and ultraviolet photoelectron spectroscopy (UPS) measurements conducted using an Escalab QXi spectrometer (Thermo Fisher Scientific, Waltham, MA, USA). Fourier transform infrared (FTIR) spectra were collected on a Nicolet iS50 spectrometer (Thermo Fisher Scientific, Madison, WI, USA). Scanning electron microscopy (SEM) images were obtained using a Hitachi S-4800 microscope (Hitachi, Tokyo, Japan). Measurement of contact angle measurements on ETL using the JC2000D1 contact angle instrument (manufactured by Shanghai Zhongchen Digital Technology Equipment Co., Ltd., Shanghai, China). X-ray diffraction (XRD) patterns were recorded on a Rigaku D/max-ga diffractometer (Rigaku Corporation, Tokyo, Japan) with Cu K $\alpha$  radiation. ETL conductivity, electron mobility, space-charge-limited current (SCLC), current density-voltage (*J*-*V*) characteristics, and steady-state current density and PCE at maximum-power-point tracking were characterized under AM 1.5G simulated sunlight (100 mW·cm<sup>-2</sup>, Model 94043A, Oriel Instruments, Irvine, CA, USA). Photoluminescence (PL) spectra were obtained using an FLS1000 PL microscopic spectrometer (Edinburgh Instruments, UK) with a 385 nm continuous-wave laser. Optical properties were analyzed using a UV-vis spectrophotometer (Shimadzu UV-3600Plus, Shimadzu Corporation, Kyoto, Japan). Kelvin probe force microscopy (KPFM) was performed using a Bruker Icon microscope (Bruker Nano, Santa Barbara, CA, USA). Time-resolved photoluminescence (TRPL) measurements were performed on the same FLS1000 system at an excitation wavelength of 385 nm. Transient photovoltage (TPV) spectra and transient photocurrent (TPC) were measured using a CEL-TPV2000 system (CEAULIGHT Co., Ltd., Beijing, China). Electrochemical impedance spectroscopy (EIS), and Mott-Schottky was carried out using a CHI660C electrochemical workstation (Chenhua Instrument Co., Ltd., Shanghai, China). External quantum efficiency (EQE) measurements were carried out using a QE-R system (Newport PV Measurement, Shanghai, China).

### Statistical analysis

For PCE statistics, *n* = 10 devices were measured for each group: control, AA-, ABA-, and DBA-modified. Data were processed using Origin 2017.

The standard deviation (SD) was calculated using the sample standard deviation formula:

$$SD = \sqrt{\frac{\sum_{i=1}^k x_i - \bar{x}}{k - 1}}$$

where  $x_i$  = individual PCE value,  $\bar{x}$  = average PCE, and *k* = number of valid devices.

## RESULTS AND DISCUSSION

The molecular configurations of AA, ABA, and DBA are presented in [Figure 1A-C](#), and their applicability for forming interfacial SAMs is summarized in [Supplementary Figure 1](#). To elucidate molecular charge distribution, electrostatic surface potential (ESP) analysis was performed. As shown in [Figure 1D-F](#), the

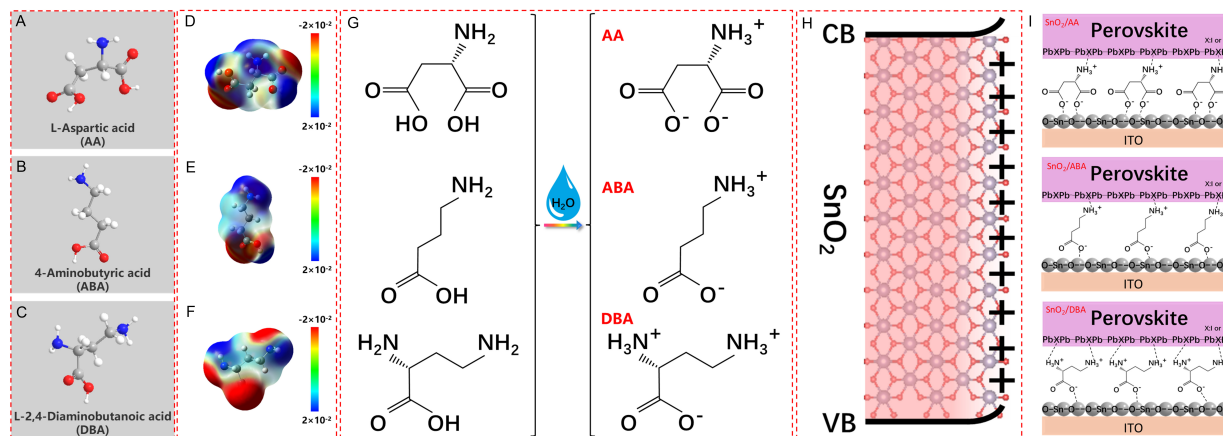


**Figure 1.** Material properties. Molecular structure and side view of (A) AA, (B) ABA, and (C) DBA. Calculated ESP of (D) AA, (E) ABA, and (F) DBA; (G) Solution states of AA, ABA, and DBA; (H) Lattice imperfections and surface states of  $\text{SnO}_2$  surfaces; (I) Schematic illustration of passivation at the  $\text{SnO}_2$ /perovskite interface using AA, ABA, and DBA. CB: Conduction band; VB: valence band; ITO: indium tin oxide.

amino group ( $-\text{NH}_2$ ) exhibits a positive ESP (blue regions) and thus acts as an EDG, while the carboxyl group ( $-\text{COOH}$ ) displays higher electron density (red regions) and serves as an EWG. Detailed atomic natural charge data are listed in [Supplementary Figure 2](#).

In solution, the EWG of dipolar molecules tends to ionize and release hydrogen ions ( $\text{H}^+$ ), becoming negatively charged. Conversely, the EDG tends to bind  $\text{H}^+$  and become positively charged [Figure 1G]<sup>[31]</sup>. The specific reaction pathways are detailed in [Supplementary Figure 3](#). The  $\text{SnO}_2$  film surface exhibits upward band bending due to lattice defects and surface states, creating a positive space-charge region (also termed an electron depletion layer) [Figure 1H]<sup>[32,33]</sup>. Upon spin-coating dipolar molecules onto the  $\text{SnO}_2$  ETL, electrostatic interactions drive molecular arrangement. Negatively charged EWGs approach the  $\text{SnO}_2$  layer, while positively charged EDGs are repelled toward the perovskite layer. Consequently, the EWGs and EDGs of dipolar molecules can passivate defects at the ETL and perovskite sides via a charge-transfer mechanism [Figure 1I]<sup>[34]</sup>.

The three types of dipolar molecules with distinct configurations exhibit different interfacial defect passivation behaviors. First, XPS and FTIR were employed to investigate chemical interactions between dipolar molecules and  $\text{SnO}_2$  films. As shown in [Figure 2A](#), an N 1s peak at 400.49 eV appears in all modified  $\text{SnO}_2$  films but is absent in the control, confirming successful deposition of modifiers on the  $\text{SnO}_2$  surface. From [Figure 2B](#), the binding energies of  $\text{Sn } 3d_{5/2}$  and  $\text{Sn } 3d_{3/2}$  shift from 486.49 and 494.91 eV (pristine  $\text{SnO}_2$ ) to 486.23 and 494.66 eV (AA-modified), 486.39 and 494.83 eV (ABA-modified), and 486.45 and 494.85 eV (DBA-modified), respectively. Deconvolution of the O 1s peaks [Figure 2C] reveals two components: lattice oxygen ( $\text{O}_L$ ) at lower binding energy and oxygen vacancies ( $\text{O}_V$ ) at higher binding energy. The relative concentration of  $\text{O}_V$ , calculated using  $R_{OV} = S_{OV} / (S_{OV} + S_{OL})$ , where  $S_{OL}$  and  $S_{OV}$  are the corresponding peak areas<sup>[35]</sup>, yields values of 0.32, 0.09, 0.13, and 0.19 for the control, AA-, ABA-, and DBA-modified  $\text{SnO}_2$  films, respectively. These results confirm effective passivation of  $\text{O}_V$  defects after modification. [Figure 2D](#) displays FTIR spectra of control and modified  $\text{SnO}_2$  films in the 1,200–1,800  $\text{cm}^{-1}$  region. After chemical interaction with  $\text{SnO}_2$ , the C–O stretching peak in the dipolar molecules shifts: 1,246→1,240  $\text{cm}^{-1}$  (AA→AA-modified), 1,246→1,244  $\text{cm}^{-1}$  (ABA→ABA-modified), and 1,245→1,244  $\text{cm}^{-1}$  (DBA→DBA-modified). The C=O stretching peaks of AA (1,669  $\text{cm}^{-1}$ ), ABA (1,674  $\text{cm}^{-1}$ ), and DBA (1,677  $\text{cm}^{-1}$ ) shift to higher wavenumbers in the modified films: 1,706  $\text{cm}^{-1}$  (AA), 1,694  $\text{cm}^{-1}$  (ABA), and 1,696  $\text{cm}^{-1}$  (DBA). These results verify chemical interactions between the  $-\text{COO}^-$  groups of dipolar molecules and the  $\text{SnO}_2$  film. Furthermore, the strength of



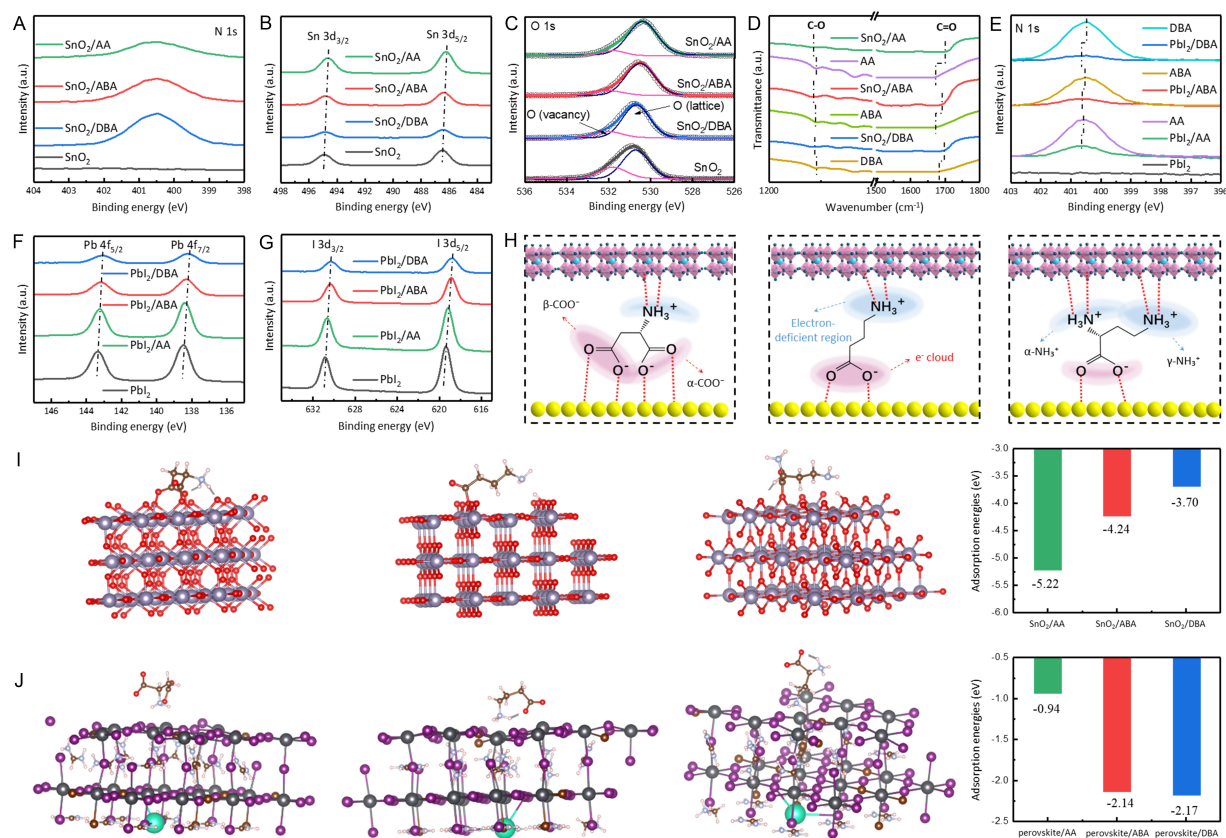


**Figure 2.** Interactions between dipolar molecules and SnO<sub>2</sub>/perovskite films. (A) N 1s, (B) Sn 3d, (C) O 1s XPS spectra, and (D) FTIR spectra of control, AA-, ABA-, and DBA-modified SnO<sub>2</sub> films. XPS spectra of (E) N 1s, (F) Pb 4f, and (G) I 3d for control, AA-, ABA-, and DBA-modified perovskite films; (H) Schematic comparison of interaction strengths of AA, ABA, and DBA with SnO<sub>2</sub> and perovskite films; (I) Coordination geometry and adsorption energy of -COO<sup>-</sup> from AA, ABA, and DBA on SnO<sub>2</sub> films; (J) Coordination geometry and adsorption energy of -NH<sub>3</sub><sup>+</sup> from AA, ABA, and DBA on perovskite films. XPS: X-ray photoelectron spectroscopy; FTIR: Fourier transform infrared; AA: L-aspartic acid; ABA: 4-aminobutyric acid; DBA: L-2,4-diaminobutyric acid.

these interactions ( $2\text{Sn}^{4+} + -\text{COO}^- \rightarrow \text{Sn}^{4+} \cdots \text{O}-\text{C}-\text{O} \cdots \text{Sn}^{4+}$ ) decreases sequentially with increasing EDG/EWG ratio. We attribute the passivation effect of -COO<sup>-</sup> groups on SnO<sub>2</sub> to their polarity. In balanced dipolar molecules, the 1:1 ratio between -COO<sup>-</sup> and -NH<sub>3</sub><sup>+</sup> results in a stable electron cloud distribution. In contrast, EDG-rich dipolar molecules carry an overall positive charge, in which  $\alpha\text{-NH}_3^+$  withdraws electron density from -COO<sup>-</sup> (shielding effect)<sup>[36–38]</sup>, weakening coordination toward Sn<sup>4+</sup>. Meanwhile, EWG-rich dipolar molecules are negatively charged, and both  $\alpha\text{-COO}^-$  and  $\beta\text{-COO}^-$  provide strong passivation via a synergistic effect. Thus, the polarity of -COO<sup>-</sup> follows the order: EWG-rich > balanced > EDG-rich. Electrical conductivity derived from current density-voltage (*I*-*V*) curves shows progressive enhancement for SnO<sub>2</sub> films treated with different modifiers, following the trend AA > ABA > DBA > control [Supplementary Figure 4]. Electron mobility exhibits the same trend [Supplementary Figure 5, Supplementary Note 1], which is inversely consistent with the variation in *O<sub>v</sub>* defect concentration within SnO<sub>2</sub> films.

Next, chemical interactions between the three dipolar molecules and perovskite films were investigated. The N 1s peaks of AA (400.55 eV), ABA (400.47 eV), and DBA (400.41 eV) shift to higher binding energies in AA-PbI<sub>2</sub> (400.61 eV), ABA-PbI<sub>2</sub> (400.59 eV), and DBA-PbI<sub>2</sub> (400.55 eV), respectively [Figure 2E]. As shown in Figure 2F, the Pb 4f peaks (4f<sub>7/2</sub> and 4f<sub>5/2</sub>) in the control film shift systematically to lower binding energies after modification with AA (138.38, 143.24 eV), ABA (138.30, 143.15 eV), and DBA (138.15, 143.04 eV), compared with the control (138.48, 143.37 eV). The I 3d<sub>3/2</sub> and I 3d<sub>5/2</sub> peaks show similar shifts [Figure 2G]. The magnitude of the low-energy shift follows the order DBA > ABA > AA, indicating that DBA forms the

strongest chemical bonds with  $\text{Pb}^{2+}/\text{I}^-$ . This trend is proportional to the EDG/EWG ratio and arises from the polarity of the EDG in the dipole molecule. The binding is dominated by Lewis acid-base coordination between the nitrogen lone pair in  $-\text{NH}_3^+$  and  $\text{Pb}^{2+}$ , as well as  $\text{N}-\text{H}\cdots\text{I}$  hydrogen bonding between  $-\text{NH}_3^+$  and iodide in the perovskite lattice<sup>[39]</sup>.

As shown in Figure 2H, EWG-rich and EDG-rich dipolar molecules exhibit complementary passivation effects on  $\text{SnO}_2$  and perovskite: EWG-rich dipolar molecules passivate  $\text{SnO}_2$  more effectively but are less efficient for perovskite, while EDG-rich dipolar molecules show the opposite behavior. First-principles DFT calculations further evaluate the interaction mechanisms at the atomic scale. The calculated adsorption energies ( $E_{\text{ads}}$ ) for  $-\text{COO}^-$  binding on  $\text{SnO}_2$  are -5.22 eV (AA), -4.24 eV (ABA), and -3.70 eV (DBA) [Figure 2I]. For  $-\text{NH}_3^+$  binding on perovskite, the corresponding  $E_{\text{ads}}$  values are -0.94 eV (AA), -2.14 eV (ABA), and -2.17 eV (DBA) [Figure 2J], consistent with the analysis in Figure 2H. Therefore, by identifying which molecular structure yields superior device performance, we can determine which interface dominates performance limitation at the buried interface.

Top-view SEM was used to analyze morphological differences between control and modified perovskite films. From Figure 3A, the perovskite grain size follows the order: control (606 nm) < AA (758 nm) < ABA (739 nm) < DBA (1,058 nm) [Supplementary Figure 6]. Cross-sectional SEM images show a similar trend [Figure 3B]. The crystal structures of perovskite films on different substrates were further characterized by XRD. As shown in Supplementary Figure 7, all films display characteristic perovskite peaks at  $14.1^\circ$  and  $28.6^\circ$ , corresponding to the (110) and (220) planes, respectively. Modified  $\text{SnO}_2$  substrates enhance the diffraction intensities, which correlate positively with the EDG/EWG ratio. Subsequent exfoliation experiments reveal how the three dipole configurations affect the perovskite buried interface [Figure 3C]. The pinhole density at the buried interface correlates negatively with the EDG/EWG ratio.

To understand the improved crystal quality, contact angles of  $\text{SnO}_2$  films and *in situ* temperature-dependent XRD were measured. The contact angles of the perovskite precursor solution on control, AA-, ABA-, and DBA-modified  $\text{SnO}_2$  films are  $19.81^\circ$ ,  $14.39^\circ$ ,  $12.55^\circ$ , and  $7.49^\circ$ , respectively [Figure 3D]. Compared with the control, modified perovskite films show a slower increase in (110) diffraction intensity with rising temperature, and this effect becomes more pronounced with increasing EDG/EWG ratio [Figure 3E]. This behavior is mainly attributed to the stronger polarity of EDG moieties and higher hydrophilicity of dipolar molecules with larger EDG/EWG ratios, which strengthen coordination with perovskite precursors, especially  $\text{Pb}^{2+}$  in  $\text{PbI}_2$ . This chelation immobilizes free  $\text{Pb}^{2+}$  ions and favors the formation of a stable  $\text{PbI}_2\text{-NH}_3^+$  intermediate at the buried interface. This effect promotes rapid nucleation while slowing the overall crystallization rate. The underlying reason is that  $\text{PbI}_2$  anchored at the buried interface requires additional time to be released and incorporated into the perovskite lattice. A reduced contact angle and retarded crystallization promote uniform spreading of the perovskite precursor, minimize pinhole defects, and facilitate the formation of large grains<sup>[40]</sup>.

Improved crystallization helps reduce internal stress in films. Depth-dependent grazing-incidence X-ray diffraction (GIXRD) measurements were performed at multiple incident angles ( $\psi = 7^\circ, 9^\circ, 11^\circ, 13^\circ, 15^\circ$ ) to probe stress distribution at different depths [Figure 4A-D]<sup>[41]</sup>. The (211) diffraction peak was chosen for analysis due to its higher angle, which provides more accurate structural information<sup>[42]</sup>. As the incident angle increases, the compressive-stress (211) peak gradually shifts to lower angles in both control and modified films, indicating lattice contraction. Notably, the magnitude of this low angle shift correlates negatively with the EDG/EWG ratio, which originates from improved perovskite crystallinity [Supplementary Figure 8]. Reduced internal stress results in fewer defects. SCLC measurements reveal the trap density [Figure 4E]. The trap-filled limit voltage is suppressed from 0.928 V (control) to 0.869 V (AA),

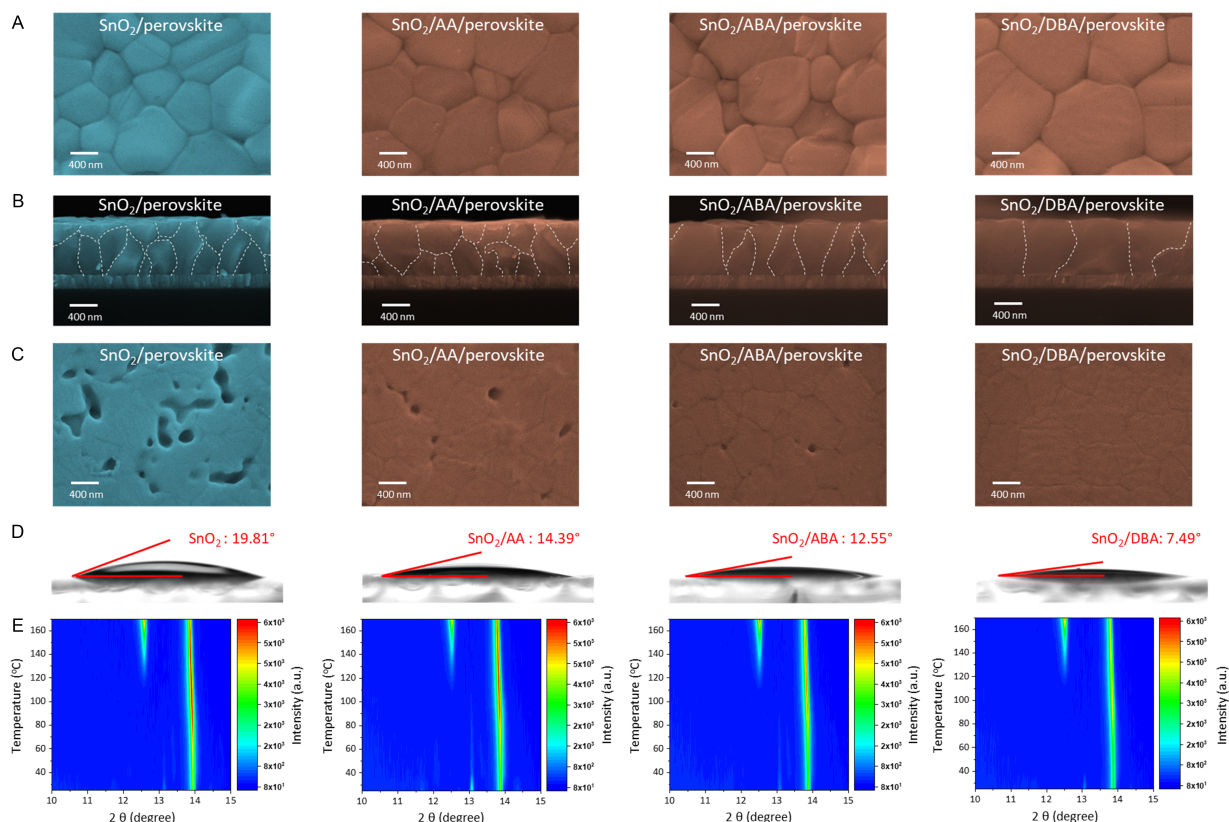


**Figure 3.** Perovskite films grown on control, AA-, ABA-, and DBA-modified SnO<sub>2</sub> films. (A) Top-view, (B) cross-sectional, and (C) buried-interface SEM images of control, AA-, ABA- and DBA-modified perovskite films; (D) Contact angle measurements of control, AA-, ABA-, and DBA-modified SnO<sub>2</sub> films; (E) *In situ* temperature-dependent XRD contours of control, AA-, ABA- and DBA-modified perovskite films. AA: L-aspartic acid; ABA: 4-aminobutyric acid; DBA: L-2,4-diaminobutyric acid; SEM: scanning electron microscopy; XRD: X-ray diffraction.

0.638 V (ABA), and 0.298 V (DBA). Based on the Mott-Gurney law [Supplementary Note 2]<sup>[43]</sup>, the calculated defect densities are  $8.61 \times 10^{15} \text{ cm}^{-3}$  (DBA),  $1.84 \times 10^{16} \text{ cm}^{-3}$  (ABA),  $2.51 \times 10^{16} \text{ cm}^{-3}$  (AA), and  $2.68 \times 10^{16} \text{ cm}^{-3}$  (control). This trend inversely correlates with the PL intensity, which is strongest for DBA [Figure 4F]. Absolute-intensity photoluminescence (AIPL) measurements were used to determine photoluminescence quantum yield (PLQY) [Supplementary Figure 9]. The highest PLQY appears in the DBA-modified film (12.52%), followed by the ABA-modified film (11.70%) and the AA-modified film (10.76%), all of which are higher than that of the control film (5.51%). These results confirm that modified SnO<sub>2</sub> layers suppress non-radiative recombination, and the suppression effect increases with the EDG/EWG ratio. The EDG-rich dipolar molecules-modified perovskite films exhibit the lowest defect density and most effectively suppress non-radiative recombination.

Interfacial energy-level alignment in dipolar molecules-modified SnO<sub>2</sub> films was analyzed using UV-vis absorption spectroscopy and UPS [Figure 5A-D]. As summarized in Supplementary Table 1, the bandgap ( $E_g$ ) of control, DBA-, ABA-, and AA-modified SnO<sub>2</sub> films increases gradually, while the Fermi level ( $E_F$ ) shifts upward. The valence band maximum ( $E_{VBM}$ ) and conduction band minimum ( $E_{CBM}$ ) show corresponding upward shifts. Based on these results, Figure 5E illustrates the energy-level alignment in PSCs. The favorable  $E_{CBM}$  offset between modified SnO<sub>2</sub> and perovskite facilitates electron transport and suppresses interfacial non-radiative recombination losses<sup>[44]</sup>. KPFM further verifies the band structure [Figure 5F and G]. Dipolar molecules modification generally reduces the  $E_F$  of SnO<sub>2</sub>, and the magnitude of this reduction intensifies as the EDG/EWG ratio decreases. The mechanism can be explained as follows: in DBA, ABA, and

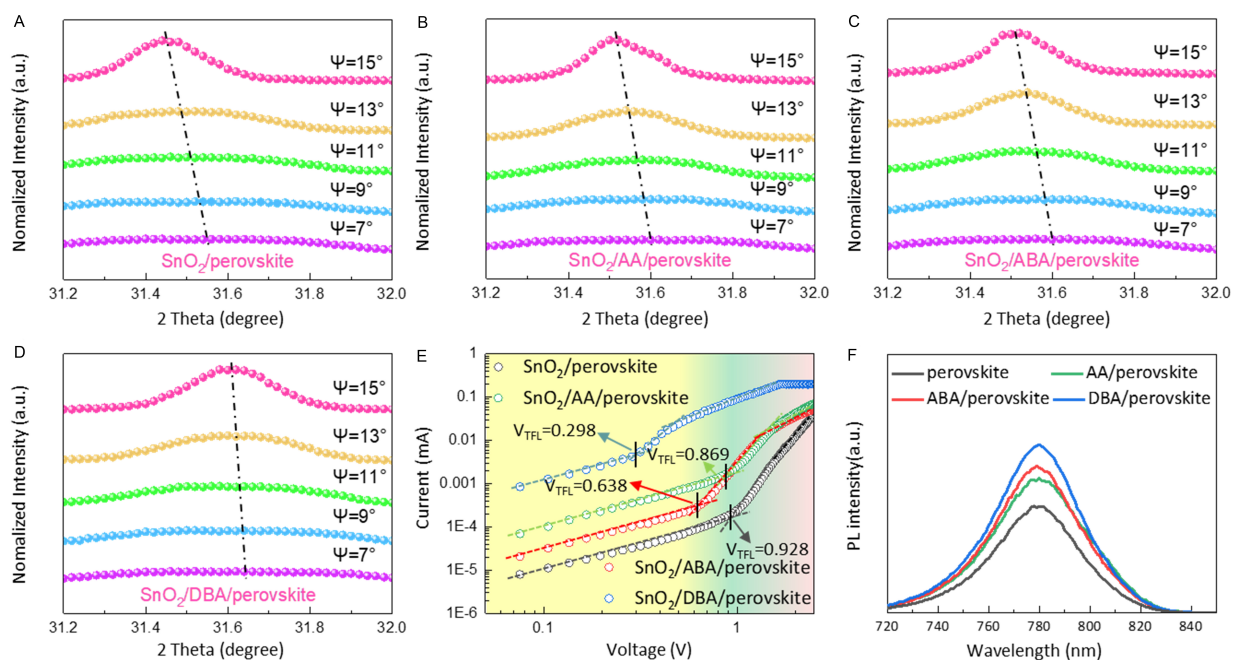


**Figure 4.** Release of residual strain in perovskite films. GIXRD patterns of (A) control, (B) AA-, (C) ABA-, and (D) DBA-modified perovskite films; (E) SCLC measurements of electron-only devices; (F) PL spectra of control, AA-, ABA-, and DBA-modified perovskite films. GIXRD: Grazing-incidence X-ray diffraction; AA: L-aspartic acid; ABA: 4-aminobutyric acid; DBA: L-2,4-diaminobutyric acid; SCLC: space-charge-limited current; PL: photoluminescence.

AA molecules, the electron cloud density of  $-\text{COO}^-$  increases sequentially. Higher electron density leads to stronger electron injection into the  $\text{SnO}_2$  surface, increasing surface electron concentration and pushing  $E_F$  toward the conduction band. Thus, a lower EDG/EWG ratio shifts  $E_F$  of  $\text{SnO}_2$  closer to the conduction band<sup>[44]</sup>. These results indicate that EWG-rich dipolar molecules-modified  $\text{SnO}_2$  exhibits better energy-level alignment with perovskite.

Cross-sectional KPFM was used to analyze electric-field distribution at the ETL/perovskite interface. The contrast at the interface correlates positively with the EDG/EWG ratio [Figure 6A]. Contact potential difference (CPD) profiles show that the interfacial potential difference increases sequentially from control to AA, ABA, and DBA, indicating enhanced electric-field strength [Figure 6B]<sup>[45–56]</sup>. From photocurrent density ( $J_{ph}$ ) versus effective voltage ( $V_{eff}$ ) measurements, the  $J_{ph}/J_{sat}$  ratio under short-circuit conditions increases gradually with rising EDG/EWG ratio [Figure 6C, Supplementary Note 3], with key parameters listed in Supplementary Table 2. A larger  $J_{ph}/J_{sat}$  ratio indicates higher charge-collection efficiency and a stronger interfacial electric field<sup>[57]</sup>. PL and TRPL spectroscopy were used to probe charge transfer. Compared with the control, all three dipolar modifications reduce PL intensity and carrier lifetime. Notably, PL intensity correlates negatively with the EDG/EWG ratio [Figure 6D]. The average carrier lifetime decreases from 162.00 ns (control) to 139.66 ns (AA), 90.77 ns (ABA), and 3.35 ns (DBA) [Figure 6E], indicating accelerated interfacial electron extraction. Fitting parameters are listed in Supplementary Table 3. TPC and TPV were used to study charge extraction and recombination. As shown in Figure 6F, TPC results show shorter carrier extraction lifetimes for AA- (3.46  $\mu\text{s}$ ), ABA- (2.54  $\mu\text{s}$ ), and DBA-modified (2.01  $\mu\text{s}$ ) devices compared with the control (4.69  $\mu\text{s}$ ), confirming improved charge extraction and transfer, consistent with TRPL. TPV results [Supplementary Figure 10] show carrier lifetimes of 22  $\mu\text{s}$  (control), 94  $\mu\text{s}$  (AA), 106  $\mu\text{s}$  (ABA), and 118  $\mu\text{s}$  (DBA), demonstrating suppressed non-radiative recombination. Further, Mott-Schottky analysis [Figure 6G] reveals built-in potentials ( $V_{bi}$ ) of 0.82 V (control), 0.87 V (AA), 0.94 V (ABA), and 1.04 V (DBA). A higher  $V_{bi}$  provides a stronger driving force for charge dissociation and separation, directly contributing to a higher



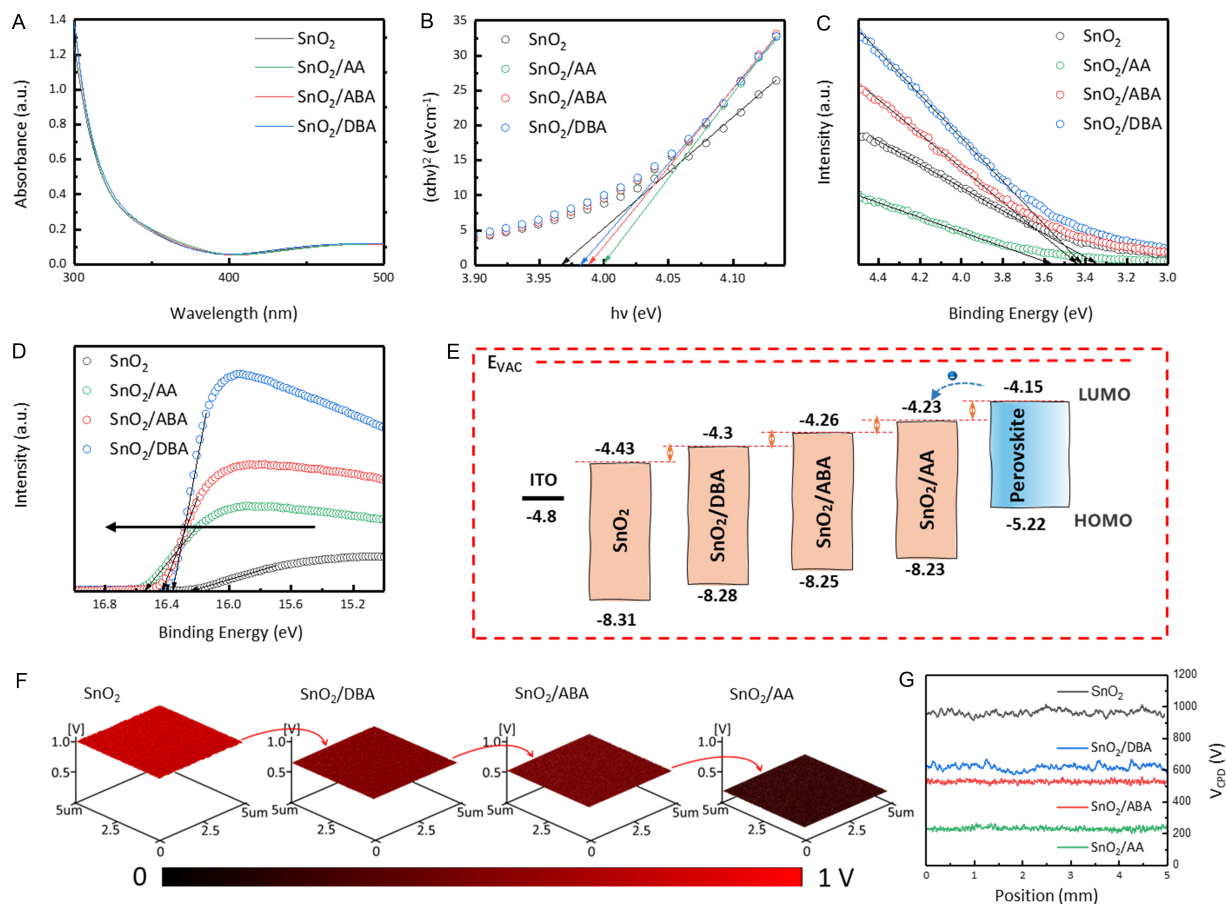


**Figure 5.** Charge-transfer kinetics at the  $\text{SnO}_2$ /perovskite interface. (A) UV-vis absorption spectra and (B) corresponding Tauc plots. UPS data for (C) secondary electron cutoff and (D) valence band region; (E) Energy-level alignment diagram; (F) KPFM images and (G) contact potential difference (CPD) values. UV-vis: Ultraviolet-visible; UPS: ultraviolet photoelectron spectroscopy; KPFM: Kelvin probe force microscopy; AA: L-aspartic acid; ABA: 4-aminobutyric acid; DBA: L-2,4-diaminobutyric acid.

$V_{oc}$  [58]. Collectively, the interfacial electric-field strength correlates positively with the EDG/EWG ratio. This is because the perovskite layer always serves as the source for the generation of electron-hole pairs. Defects at the buried interface trap charges and introduce parasitic capacitance, weakening the electric field. EDG-rich SAMs significantly enhance the electric field for two main reasons: first, a higher EDG/EWG ratio improves passivation on the perovskite side, eliminating defect-induced capacitance; second, EDG-rich dipolar molecules form positively charged SAMs that attract photogenerated electrons toward the interface and provide additional binding sites and transport channels. This facilitates electron transfer from perovskite to ETL, suppresses charge accumulation, and reduces electron-hole recombination. The synergistic effect significantly improves charge-extraction efficiency.

Fabricated  $\text{SnO}_2$  ETL devices served to evaluate the influence of three configurationally distinct dipolar molecules on photovoltaic performance [Figure 7A]. The typical  $J$ - $V$  curves of the control, AA-, ABA-, and DBA-modified devices are shown in Figure 7B, with corresponding parameters summarized in Supplementary Table 4. Compared with the champion control device ( $PCE$ : 20.05%,  $V_{oc}$ : 1.16 V,  $J_{sc}$ : 23.61  $\text{mA}\cdot\text{cm}^{-2}$ ,  $FF$ : 0.73), the champion AA-, ABA-, and DBA-modified devices achieve  $PCE$ s of 22.18% ( $V_{oc}$ : 1.19 V,  $J_{sc}$ : 24.03  $\text{mA}\cdot\text{cm}^{-2}$ ,  $FF$ : 0.78), 23.75% ( $V_{oc}$ : 1.20 V,  $J_{sc}$ : 24.82  $\text{mA}\cdot\text{cm}^{-2}$ ,  $FF$ : 0.80), and 24.18% ( $V_{oc}$ : 1.20 V,  $J_{sc}$ : 24.99  $\text{mA}\cdot\text{cm}^{-2}$ ,  $FF$ : 0.80), respectively. Statistical distributions are shown in Supplementary Figure 11 and Figure 7C. As the EDG/EWG ratio increases, average device parameters improve gradually. The enhanced  $V_{oc}$  is mainly attributed to improved perovskite film quality and reduced defect density. The increased  $J_{sc}$



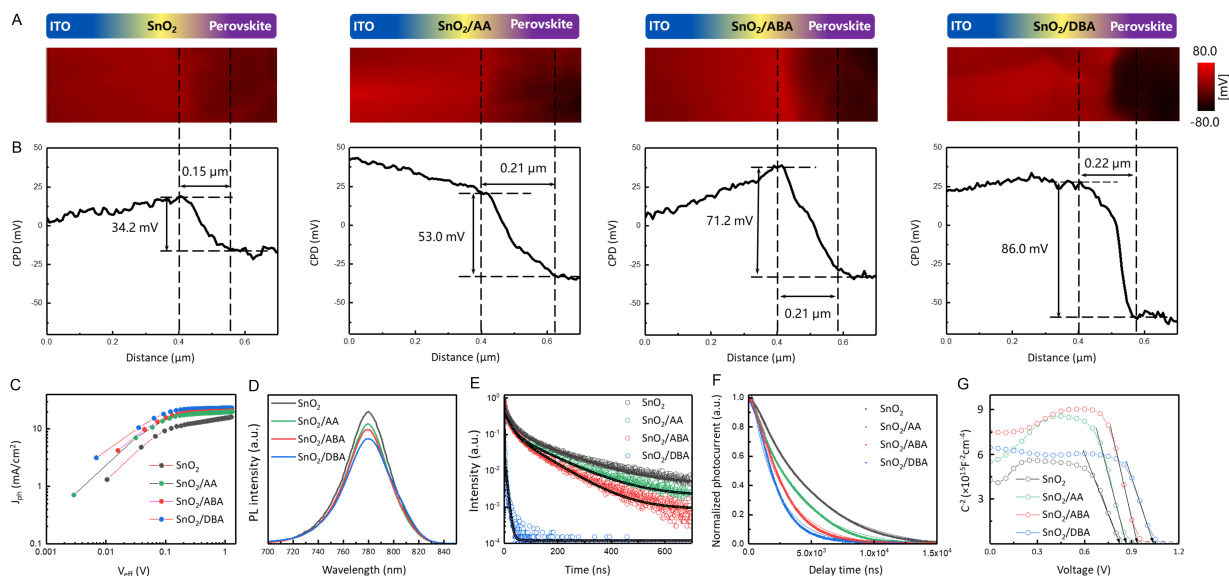


**Figure 6.** Electrical characteristics. (A) Cross-sectional KPFM images, (B) CPD profiles, and (C)  $J_{ph}$ - $V_{eff}$  curves of control, AA-, ABA-, and DBA-modified devices; (D) PL and (E) TRPL spectra of control, AA-, ABA-, and DBA-modified perovskite films; (F) TPC curves and (G) Mott-Schottky plots for control, AA-, ABA-, and DBA-modified devices. KPFM: Kelvin probe force microscopy; CPD: contact potential difference; AA: L-aspartic acid; ABA: 4-aminobutyric acid; DBA: L-2,4-diaminobutyric acid; PL: photoluminescence; TRPL: time-resolved photoluminescence; TPC: transient photocurrent; ITO: indium tin oxide.

arises from the strong interfacial electric field induced by EDG-rich dipolar molecules, which promotes efficient electron extraction. EDG-rich dipolar molecules effectively passivate perovskite but show limited passivation of  $\text{SnO}_2$ , while generating the strongest interfacial dipole field. In contrast, EWG-rich dipolar molecules effectively passivate  $\text{SnO}_2$  but weakly passivate perovskite. Although EWG-rich dipolar molecules-modified  $\text{SnO}_2$  shows better energy-level alignment with perovskite, it generates the weakest interfacial dipole field. Combined with the superior PCE of EDG-rich dipolar molecules-modified devices, we confirm that improving the perovskite interface is more decisive for overall performance than optimizing the ETL, since perovskite is the photoactive layer where electron-hole pairs are generated.

EIS measurements were performed to analyze the charge transport and recombination dynamics. Figure 7D presents Nyquist plots. As the EDG/EWG ratio increases, charge-transfer resistance ( $R_{ct}$ ) in the high-frequency region gradually decreases, while charge-recombination resistance ( $R_{rec}$ ) in the low-frequency region increases<sup>[59]</sup>. The equivalent circuit is shown in Supplementary Figure 12. The reduced  $R_{ct}$  is attributed to the enhanced interfacial electric field, while suppressed non-radiative recombination arises from reduced defect density on the perovskite side. The EQE spectrum, shown in Figure 7E, demonstrated an improved EQE for the modified devices across the entire wavelength range of 300–900 nm. The integrated  $J_{sc}$  values derived from the EQE spectra are 23.10, 23.20, 23.29, and 23.47  $\text{mA}\cdot\text{cm}^{-2}$  for control, AA-, ABA-, and DBA-modified devices, respectively, consistent with  $J_{sc}$  trends. Open-circuit voltage decay (OCVD) results [Figure 7F] indicate suppressed charge recombination. The interfacial recombination rate correlates negatively with the EDG/EWG ratio, while carrier lifetime increases. Dark  $J$ - $V$  curves [Figure 7G] show reduced dark current with increasing EDG/EWG ratio under both forward and reverse bias, indicating enhanced shunt resistance.

Supplementary Figure 13 shows steady-state current density and PCE under maximum-power-point tracking. After 200 s, the control, AA-, ABA-, and DBA-modified devices yield steady-state current densities of 22.89, 23.19, 24.37, and 24.41  $\text{mA}\cdot\text{cm}^{-2}$ , with steady-state PCEs of 19.53%, 21.57%, 23.32%, and 23.72%, respectively. Long-term stability is critical for commercialization<sup>[60–62]</sup>. First, the four types of films were aged

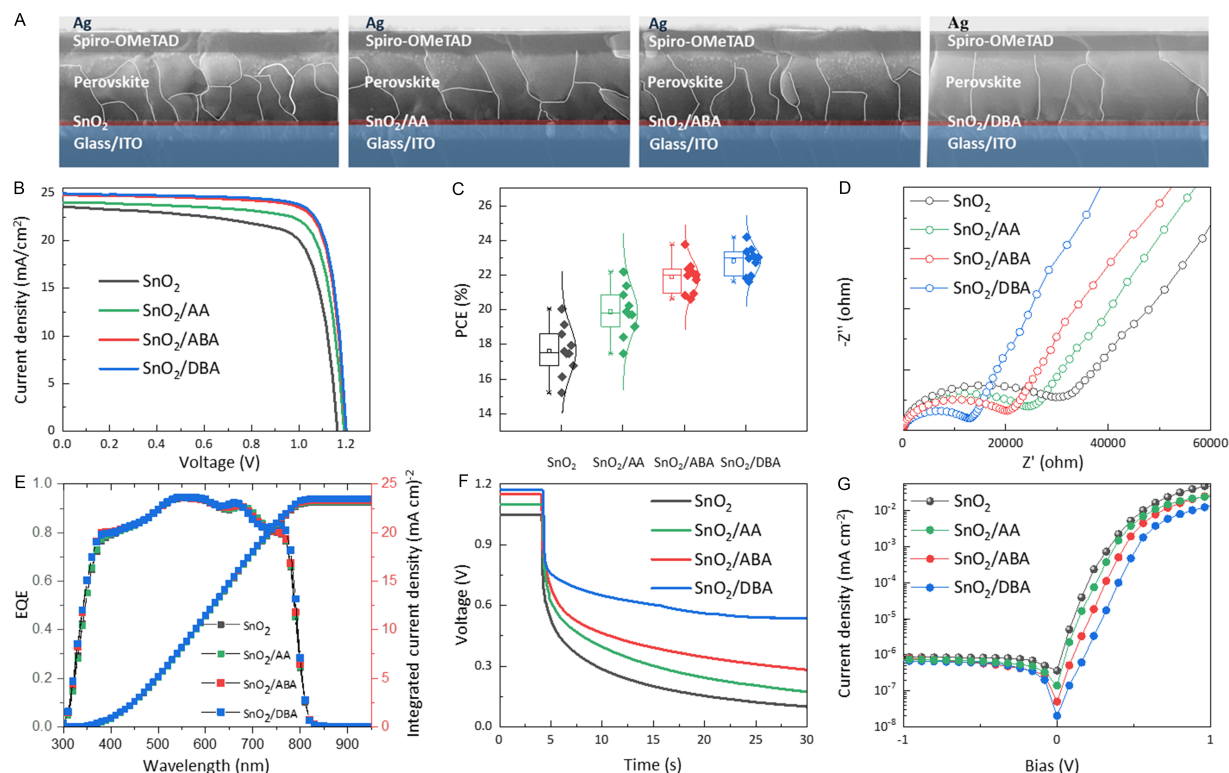


**Figure 7.** Photovoltaic performance of PSCs. (A) Cross-sectional SEM images; (B)  $J$ - $V$  curves under 1 sun illumination; (C) PCE statistics; (D) Nyquist plots in the dark; (E) EQE spectra; (F) OCVD curves; (G) Dark  $J$ - $V$  curves for control, AA-, ABA-, and DBA-modified devices. PSCs: Perovskite solar cells; SEM: scanning electron microscopy; PCE: power conversion efficiency; EQE: external quantum efficiency; OCVD: open-circuit voltage decay; AA: L-aspartic acid; ABA: 4-aminobutyric acid; DBA: L-2,4-diaminobutyric acid; Spiro-OMeTAD: 2,2',7,7'-tetrakis(N,N-di-p-methoxyphenylamine)-9,9'-spirobifluorene; ITO: indium tin oxide.

for 28 days in an air environment at 25–30 °C with a relative humidity (RH) of 30%. [Supplementary Figure 14A](#) shows photographs after aging; degradation decreases in the order control > AA > ABA > DBA. XRD patterns [[Supplementary Figure 14B](#)] confirm that the control perovskite decomposes significantly, with a strong PbI<sub>2</sub> peak at 12.6°, while DBA-modified film remains almost unchanged. Under high-temperature and high-humidity conditions (85 °C, 85% RH) for 72 h, the color transition from black to yellow is alleviated in the same order [[Supplementary Figure 15](#)], confirming improved thermal and moisture stability for DBA-modified film. Device stability was further evaluated. Under 65% RH at room temperature [[Supplementary Figure 16A](#)], the control device retains only 48.81% of its initial PCE after 720 h, while AA-, ABA-, and DBA-modified devices maintain 68.79%, 72.62%, and 80.14%, respectively. Under thermal aging in N<sub>2</sub> [[Supplementary Figure 16B](#)], the DBA-modified device retains over 82.14% after 120 h, higher than 57.86% (control), 73.86% (AA), and 78.63% (ABA). Under continuous light soaking (100 mW·cm<sup>-2</sup>) in N<sub>2</sub> for 60 h [[Supplementary Figure 16C](#)], DBA retains 75.14%, while control, AA, and ABA drop to 47.36%, 65.36%, and 70.63%. For long-term ambient storage (20–25 °C, 25%–30% RH, [Supplementary Figure 16D](#)), the DBA-modified device retains more than 85.25% after 30 days, compared with 60.07% (control), 69.68% (AA), and 75.05% (ABA). These results demonstrate that modified SnO<sub>2</sub> layers enhance stability, and the improvement scales with the EDG/EWG ratio. Enhanced stability is attributed to improved crystallinity and reduced buried-interface defects, which hinder oxygen and moisture penetration. EWG-rich dipolar molecules most effectively remove SnO<sub>2</sub> surface defects and hydroxyl groups, suppressing interfacial deprotonation. EDG-rich dipolar molecules most significantly reduce perovskite grain boundary density, retarding moisture-induced degradation. Combined with the superior stability of EDG-rich dipolar molecules-modified devices, we confirm that passivation of the perovskite surface dominates device stability more than ETL modification.

## CONCLUSION

In summary, this work provides a clear strategy for buried interface engineering in perovskite solar cells. Since the perovskite layer acts as the photoactive layer where electron-hole pairs are generated, whereas  $\text{SnO}_2$  serves only as an ETL, passivation of the perovskite surface is far more critical than modification of the  $\text{SnO}_2$  layer. Accordingly, EDG-rich dipolar molecules, rather than EWG-rich ones, play a decisive role in regulating buried interface properties, and a higher EDG/EWG ratio is essential for achieving optimal interface modification. A lower EDG/EWG ratio strengthens the electron-withdrawing ability of the molecules, which helps passivate defects in the  $\text{SnO}_2$  film and optimize energy-level alignment, but also introduces negative surface charges that repel electrons and limit performance. In contrast, a higher EDG/EWG ratio enhances the electron-donating characteristics and promotes stronger interactions with  $\text{PbI}_2$ . EDG-rich dipolar molecules-modified  $\text{SnO}_2$  films show improved wettability, retarded perovskite crystallization, enhanced film uniformity and crystallinity, and more effective strain release. These molecules also carry positive surface charges, provide more sites for electron extraction, and generate a stronger interfacial dipole moment, all of which facilitate efficient electron extraction. As a result, DBA-modified devices yield a champion PCE of 24.18%, and unencapsulated devices retain more than 85% of their initial efficiency after 30 days in ambient conditions. This work establishes a clear design principle for interface modifier molecules: effective passivation of both ETL and perovskite is desirable, but passivation of the perovskite surface is dominant. Future interface molecules should emphasize strong electron-donating characteristics and a positive dipole moment to maximize synergy with the perovskite layer, guiding the development of more efficient and stable perovskite solar cells.

## DECLARATIONS

### Authors' contributions

Writing - original draft, methodology, data curation: Duan, H.  
Software, methodology: Jin, J.  
Software, data curation: Liu, X.  
Methodology, investigation: Yang, X.  
Validation, resources: Liu, H.  
Resources, investigation: Fan, L.  
Writing - review and editing, supervision, conceptualization: Wang, F.  
Project administration, funding acquisition, formal analysis: Yang, J.  
Visualization, validation, software: Yang, L.

### Availability of data and materials

Some data are presented in the “[Supplementary Materials](#)” section. Other raw data that support the findings of this study are available from the corresponding author upon reasonable request.

### AI and AI-assisted tools statement

Not applicable.

### Financial support and sponsorship

This work was supported by the National Natural Science Foundation of China (Nos. 62275101 and 22075101), Program for the Development of Science and Technology of Jilin province (No. YDZJ202401346ZYTS), Program for the Science and Technology of Education Department of Jilin Province (No. JJKH20250934BS).

### Conflicts of interest

All authors declared that there are no conflicts of interest.

### Ethical approval and consent to participate

Not applicable.

**Consent for publication**

Not applicable.

**Copyright**

© The Author(s) 2026.

**Supplementary Materials**

[Supplementary Materials](#)

**REFERENCES**

1. Fan, Y.; Qin, Z.; Lu, L.; et al. An efficient and precise solution-vacuum hybrid batch fabrication of 2D/3D perovskite submodules. *Nat. Commun.* **2025**, *16*, 7019. [DOI PubMed PMC](#)
2. Li, Q.; Liu, H.; Hou, C.; et al. Harmonizing the bilateral bond strength of the interfacial molecule in perovskite solar cells. *Nat. Energy.* **2024**, *9*, 1506-16. [DOI](#)
3. Xu, H.; Xiao, Y.; Elmostekawy, K. A.; et al. Metastable interphase induced pre-strain compensation enables efficient and stable perovskite solar cells. *Energy. Environ. Sci.* **2025**, *18*, 246-55. [DOI](#)
4. Xu, R.; Wang, C.; Zhang, Z.; et al. Buried interface engineering: a key to unlocking the potential of self-assembled monolayer (SAM)-based inverted perovskite solar cells. *Small* **2025**, *21*, e2503114. [DOI PubMed](#)
5. Bi, H.; Zuo, X.; Liu, B.; et al. Multifunctional organic ammonium salt-modified SnO<sub>2</sub> nanoparticles toward efficient and stable planar perovskite solar cells. *J. Mater. Chem. A.* **2021**, *9*, 3940-51. [DOI](#)
6. Wei, K.; Yang, L.; Deng, J.; Luo, Z.; Zhang, X.; Zhang, J. Facile exfoliation of the perovskite thin film for visualizing the buried interfaces in perovskite solar cells. *ACS. Appl. Energy. Mater.* **2022**, *5*, 7458-65. [DOI](#)
7. Wang, L.; Xia, J.; Yan, Z.; et al. Robust interfacial modifier for efficient perovskite solar cells: reconstruction of energy alignment at buried interface by self-diffusion of dopants. *Adv. Funct. Mater.* **2022**, *32*, 2204725. [DOI](#)
8. Wu, M.; Duan, Y.; Yang, L.; et al. Multifunctional small molecule as buried interface passivator for efficient planar perovskite solar cells. *Adv. Funct. Mater.* **2023**, *33*, 2300128. [DOI](#)
9. Deng, C.; Wu, J.; Yang, Y.; et al. Modulating residual lead iodide via functionalized buried interface for efficient and stable perovskite solar cells. *ACS. Energy. Lett.* **2022**, *8*, 666-76. [DOI](#)
10. Ge, Y.; Ye, F.; Xiao, M.; et al. Internal encapsulation for lead halide perovskite films for efficient and very stable solar cells. *Adv. Energy. Mater.* **2022**, *12*, 2200361. [DOI](#)
11. Xiong, Q.; Wang, C.; Zhou, Q.; et al. Rear interface engineering to suppress migration of iodide ions for efficient perovskite solar cells with minimized hysteresis. *Adv. Funct. Mater.* **2021**, *32*, 2107823. [DOI](#)
12. Li, H.; Xie, G.; Wang, X.; et al. Buried interface dielectric layer engineering for highly efficient and stable inverted perovskite solar cells and modules. *Adv. Sci.* **2023**, *10*, e2300586. [DOI PubMed PMC](#)
13. Chen, Y.; Zuo, X.; He, Y.; et al. Dual passivation of perovskite and SnO<sub>2</sub> for high-efficiency MAPbI<sub>3</sub> perovskite solar cells. *Adv. Sci.* **2021**, *8*, 2001466. [DOI PubMed PMC](#)
14. Xia, H.; Li, X.; Zhou, J.; et al. Interfacial chemical bridge constructed by zwitterionic sulfamic acid for efficient and stable perovskite solar cells. *ACS. Appl. Energy. Mater.* **2020**, *3*, 3186-92. [DOI](#)
15. Kim, G.; Choi, Y.; Choi, H.; Min, J.; Park, T.; Song, S. Novel cathode interfacial layer using creatine for enhancing the photovoltaic properties of perovskite solar cells. *J. Mater. Chem. A.* **2020**, *8*, 21721-8. [DOI](#)
16. Qin, Z.; Chen, Y.; Wang, X.; et al. Zwitterion-functionalized SnO<sub>2</sub> substrate induced sequential deposition of black-phase FAPbI<sub>3</sub> with rearranged PbI<sub>2</sub> residue. *Adv. Mater.* **2022**, *34*, e2203143. [DOI PubMed](#)
17. Geng, Q.; Jia, X.; He, Z.; et al. Interface engineering via amino acid for efficient and stable perovskite solar cells. *Adv. Mater. Interfaces.* **2022**, *9*, 2201641. [DOI](#)
18. Liu, S.; Li, J.; Xiao, W.; et al. Buried interface molecular hybrid for inverted perovskite solar cells. *Nature* **2024**, *632*, 536-42. [DOI PubMed](#)
19. Jiang, X.; Qin, S.; Meng, L.; et al. Isomeric diammonium passivation for perovskite-organic tandem solar cells. *Nature* **2024**, *635*, 860-6. [DOI PubMed](#)
20. Peng, W.; Zhang, Y.; Zhou, X.; et al. A versatile energy-level-tunable hole-transport layer for multi-composition inverted perovskite solar cells. *Energy. Environ. Sci.* **2025**, *18*, 874-83. [DOI](#)
21. Wei, Z.; Zhou, Q.; Niu, X.; et al. Surpassing 90% Shockley-Queisser  $V_{oc}$  limit in 1.79 eV wide-bandgap perovskite solar cells using bromine-substituted self-assembled monolayers. *Energy. Environ. Sci.* **2025**, *18*, 1847-55. [DOI](#)

- 
22. Gao, L.; He, Z.; Zeng, K.; Liu, A.; Jiang, F.; Ma, T. Ultralow-temperature SnO<sub>2</sub> electron transport layers fabricated by intermediate-controlled chemical bath deposition for highly efficient perovskite solar cells. *ChemSusChem* **2023**, *16*, e202300765. DOI PubMed
  23. Chen, Z.; Jiang, S.; Du, X.; et al. Three-dimensional (3D) fluoride molecular glue to improve the SnO<sub>2</sub>/perovskite interface for efficient perovskite solar cells. *Angew. Chem. Int. Ed. Engl.* **2025**, *64*, e202415669. DOI PubMed
  24. Wang, Y.; Ye, J.; Song, J.; et al. Synchronous modulation of hole-selective self-assembled monolayer and buried interface for inverted perovskite solar cells. *Cell. Rep. Phys. Sci.* **2024**, *5*, 101992. DOI
  25. Shi, C.; Wang, J.; Lei, X.; et al. Modulating competitive adsorption of hybrid self-assembled molecules for efficient wide-bandgap perovskite solar cells and tandems. *Nat. Commun.* **2025**, *16*, 3029. DOI PubMed PMC
  26. Zhou, H.; Wang, W.; Duan, Y.; et al. Glycol monomethyl ether-substituted carbazolyl hole-transporting material for stable inverted perovskite solar cells with efficiency of 25.52%. *Angew. Chem. Int. Ed. Engl.* **2024**, *63*, e202403068. DOI PubMed
  27. Torres Merino, L. V.; Petoukhoff, C. E.; Matiash, O.; et al. Impact of the valence band energy alignment at the hole-collecting interface on the photostability of wide band-gap perovskite solar cells. *Joule* **2024**, *8*, 2585-606. DOI
  28. Wang, R.; Wu, C.; Qi, J.; et al. Side-chain methylthio-based position isomerism of hole-transport materials for perovskite solar cells: from theoretical simulation to experimental characterization. *Adv. Funct. Mater.* **2023**, *33*, 2213843. DOI
  29. Farag, A.; Feeney, T.; Hossain, I. M.; et al. Evaporated self-assembled monolayer hole transport layers: lossless interfaces in *p-i-n* perovskite solar cells. *Adv. Energy Mater.* **2023**, *13*, 2203982. DOI
  30. Wei, Y.; Tang, Y.; Li, H.; et al. Decreased hysteresis benefited from enhanced lattice oxygen and promoted band alignment with electron transport layer modification in perovskite solar cells. *ACS Appl. Mater. Interfaces.* **2025**, *17*, 11278-86. DOI PubMed
  31. Chen, Q.; Yang, X.; Zhou, Y.; Song, B. Zwitterions: promising interfacial/doping materials for organic/perovskite solar cells. *New. J. Chem.* **2021**, *45*, 15118-30. DOI
  32. Liu, J.; Li, S.; Liu, S.; et al. Oxygen vacancy management for high-temperature mesoporous SnO<sub>2</sub> electron transport layers in printable perovskite solar cells. *Angew. Chem. Int. Ed. Engl.* **2022**, *61*, e202202012. DOI PubMed
  33. Mallik, N.; Hajhmati, J.; Frégnaux, M.; et al. Interface defect formation for atomic layer deposition of SnO<sub>2</sub> on metal halide perovskites. *Nano. Energy.* **2024**, *126*, 109582. DOI
  34. Fu, S.; Sun, N.; Chen, H.; et al. On-demand formation of Lewis bases for efficient and stable perovskite solar cells. *Nat. Nanotechnol.* **2025**, *20*, 772-8. DOI PubMed
  35. Zhou, Q.; He, D.; Zhuang, Q.; et al. Revealing steric-hindrance-dependent buried interface defect passivation mechanism in efficient and stable perovskite solar cells with mitigated tensile stress. *Adv. Funct. Mater.* **2022**, *32*, 2205507. DOI
  36. Kong, W.; Zhu, D.; Zhang, Y.; et al. Electron donor coordinated metal-organic framework to enhance photoelectrochemical performance. *Angew. Chem. Int. Ed. Engl.* **2023**, *62*, e202308514. DOI PubMed
  37. Wang, K.; Hong, Q.; Zhu, C.; et al. Metal-ligand dual-site single-atom nanozyme mimicking urate oxidase with high substrates specificity. *Nat. Commun.* **2024**, *15*, 5705. DOI PubMed PMC
  38. Ma, L.; Yao, H.; Wang, J.; et al. Impact of electrostatic interaction on bulk morphology in efficient donor-acceptor photovoltaic blends. *Angew. Chem. Int. Ed. Engl.* **2021**, *60*, 15988-94. DOI PubMed
  39. Zhang, L.; Cao, K.; Qian, J.; et al. Crystallization control and multisite passivation of perovskites with amino acid to boost the efficiency and stability of perovskite solar cells. *J. Mater. Chem. C.* **2020**, *8*, 17482-90. DOI
  40. Du, J.; Feng, L.; Guo, X.; et al. Enhanced efficiency and stability of planar perovskite solar cells by introducing amino acid to SnO<sub>2</sub>/perovskite interface. *J. Power. Sources.* **2020**, *455*, 227974. DOI
  41. Li, Y.; Zhao, C.; Wang, L.; et al. Self-assembled manganese acetate@tin dioxide colloidal quantum dots as an electron-transport layer for efficient and stable perovskite solar cells. *Inorg. Chem. Front.* **2024**, *11*, 3566-77. DOI
  42. Liu, B.; Zhou, Q.; Li, Y.; et al. Polydentate ligand reinforced chelating to stabilize buried interface toward high-performance perovskite solar cells. *Angew. Chem. Int. Ed. Engl.* **2024**, *63*, e202317185. DOI PubMed
  43. Li, T.; Wang, S.; Yang, J.; et al. Multiple functional groups synergistically improve the performance of inverted planar perovskite solar cells. *Nano. Energy.* **2021**, *82*, 105742. DOI
  44. Canil, L.; Cramer, T.; Fraboni, B.; et al. Tuning halide perovskite energy levels. *Energy. Environ. Sci.* **2021**, *14*, 1429-38. DOI
  45. Li, Z.; Wang, C.; Sun, P.; et al. *In-situ* peptization of WO<sub>3</sub> in alkaline SnO<sub>2</sub> colloid for stable perovskite solar cells with record fill-factor approaching the shockley-queisser limit. *Nano. Energy.* **2022**, *100*, 107468. DOI
  46. Yu, X.; Lv, Y.; Xue, B.; et al. Multiple bonding effects of 1-methanesulfonyl-piperazine on the two-step processed perovskite towards efficient and stable solar cells. *Nano. Energy.* **2022**, *93*, 106856. DOI
  47. Su, P.; Bi, H.; Ran, D.; et al. Multifunctional and multi-site interfacial buffer layer for efficient and stable perovskite solar cells. *Chem. Eng. J.* **2023**, *472*, 145077. DOI



48. Su, H.; Xu, Z.; He, X.; et al. Surface energy engineering of buried interface for highly stable perovskite solar cells with efficiency over 25. *Adv. Mater.* **2024**, *36*, e2306724. DOI PubMed
49. Xu, X.; Sun, Y.; He, D.; et al. Grain size control for high-performance formamidinium-based perovskite solar cells via suppressing heterogeneous nucleation. *J. Mater. Chem. C*. **2021**, *9*, 208–13. DOI
50. Jiang, X.; Zhang, B.; Yang, G.; et al. Molecular dipole engineering of carbonyl additives for efficient and stable perovskite solar cells. *Angew. Chem. Int. Ed. Engl.* **2023**, *62*, e202302462. DOI PubMed
51. Du, Y.; Tian, Q.; Chang, X.; et al. Ionic liquid treatment for highest-efficiency ambient printed stable all-inorganic CsPbI<sub>3</sub> perovskite solar cells. *Adv. Mater.* **2022**, *34*, e2106750. DOI PubMed
52. Aranda, C. A.; Alvarez, A. O.; Chivrony, V. S.; Das, C.; Rai, M.; Saliba, M. Overcoming ionic migration in perovskite solar cells through alkali metals. *Joule* **2024**, *8*, 241–54. DOI
53. Li, F.; Deng, X.; Shi, Z.; et al. Hydrogen-bond-bridged intermediate for perovskite solar cells with enhanced efficiency and stability. *Nat. Photonics*. **2023**, *17*, 478–84. DOI
54. Ceratti, D. R.; Zohar, A.; Kozlov, R.; et al. Eppure si muove: proton diffusion in halide perovskite single crystals. *Adv. Mater.* **2020**, *32*, e2002467. DOI PubMed
55. Zhang, Y.; Kong, T.; Xie, H.; et al. Molecularly tailored SnO<sub>2</sub>/perovskite interface enabling efficient and stable FAPbI<sub>3</sub> solar cells. *ACS. Energy. Lett.* **2022**, *7*, 929–38. DOI
56. Sun, Y.; Zhang, J.; Yu, H.; Wang, J.; Huang, C.; Huang, J. Mechanism of bifunctional p-amino benzenesulfonic acid modified interface in perovskite solar cells. *Chem. Eng. J.* **2021**, *420*, 129579. DOI
57. Lei, Y.; Li, Z.; Wang, H.; et al. Manipulate energy transport via fluorinated spacers towards record-efficiency 2D Dion-Jacobson CsPbI<sub>3</sub> solar cells. *Sci. Bull.* **2022**, *67*, 1352–61. DOI PubMed
58. Zhan, S.; Duan, Y.; Liu, Z.; et al. Stable 24.29%-efficiency FA<sub>0.85</sub>MA<sub>0.15</sub>PbI<sub>3</sub> perovskite solar cells enabled by methyl haloacetate-lead dimer complex. *Adv. Energy. Mater.* **2022**, *12*, 2200867. DOI
59. Liu, Z.; Cao, F.; Wang, M.; Wang, M.; Li, L. Observing defect passivation of the grain boundary with 2-aminoterephthalic acid for efficient and stable perovskite solar cells. *Angew. Chem. Int. Ed. Engl.* **2020**, *59*, 4161–7. DOI PubMed
60. Yang, M.; Tan, Y.; Yang, G.; et al. Chemical synergic stabilization of high Br-content mixed-halide wide-bandgap perovskites for durable multi-terminal tandemsolar cells with minimized Pb leakage. *Angew. Chem. Int. Ed.* **2025**, *64*, e202415966. DOI PubMed
61. Liu, G.; Jiang, X.; Feng, W.; et al. Synergic electron and defect compensation minimizes voltage loss in lead-free perovskite solar cells. *Angew. Chem. Int. Ed. Engl.* **2023**, *62*, e202305551. DOI PubMed
62. Liu, G.; Zhong, Y.; Feng, W.; et al. Multidentate chelation heals structural imperfections for minimized recombination loss in lead-free perovskite solar cells. *Angew. Chem. Int. Ed. Engl.* **2022**, *61*, e202209464. DOI PubMed

**Disclaimer/Publisher's Note:** All statements, opinions, and data contained in this publication are solely those of the individual author(s) and contributor(s) and do not necessarily reflect those of OAE and/or the editor(s). OAE and/or the editor(s) disclaim any responsibility for harm to persons or property resulting from the use of any ideas, methods, instructions, or products mentioned in the content.



© The Author(s) 2026. Open Access This article is licensed under a Creative Commons Attribution 4.0 International License (<https://creativecommons.org/licenses/by/4.0/>), which permits unrestricted use, sharing, adaptation, distribution and reproduction in any medium or format, for any purpose, even commercially, as long as you give appropriate credit to the original author(s) and the source, provide a link to the Creative Commons license, and indicate if changes were made.